

Thermo-electrical modelling of the ATLAS ITk Strip Detector

Graham Beck^a, Kurt Brendlinger^b, Yu-Heng Chen^b, Georg Viehhauser^c

^a*Queen Mary University of London, Mile End Road, London E1 4NS, UK*

^b*Deutsches Elektronen-Synchrotron DESY, Notkestraße 85, 22607 Hamburg*

^c*University of Oxford, Keble Rd, Oxford OX1 3RH, UK*

Abstract

In this paper we discuss the use of linked thermal and electrical network models to predict the behaviour of a complex silicon detector system. We use the silicon strip detector for the ATLAS Phase-II upgrade to demonstrate the application of such a model and its performance. With this example, a thermo-electrical model is used to test design choices, validate specifications, predict key operational parameters such as cooling system requirements, and optimize operational aspects like the temperature profile over the lifetime of the experiment. The model can reveal insights into the interplay of conditions and components in the silicon module, and it is a valuable tool for estimating the headroom to thermal runaway, all with very moderate computational effort.

Keywords: Silicon detector, Thermal runaway, Thermal management, Cooling

1. Introduction

The temperatures in silicon detector systems are critically important to their performance. Fundamentally, the leakage current of a silicon sensor has a pronounced temperature dependence

$$I \propto T_S^2 e^{-T_A/T_S}, \quad (1)$$

where T_S is the sensor temperature and $T_A \simeq 7000$ K [1]. Leakage currents in the silicon sensor can become particularly significant after irradiation, and the heat generated by these leakage currents, together with the heat from front-end electronic components on the detector, needs to be removed by a cooling system. The capability of the cooling system to remove this heat is limited by the temperature of the local cold sink (typically a circulated fluid) and the thermal impedance of the heat path between the source (electronics and sensor) and the sink. Due to the strong growth of leakage power with temperature, there is a critical temperature T_{crit} above which the heat cannot be removed quickly enough, and the detector becomes thermally unstable ('thermal runaway')¹. Understanding the thermal behaviour and the headroom to thermal runaway is crucial for the design of a silicon detector system. Even before the limit of thermal stability is reached, temperatures in silicon detector systems have a major impact on key system parameters such as power supply capacity and cable dimensions, necessitating an accurate estimate.

In addition to the silicon, there can be aspects of the front-end electronics that have a temperature dependence. In the strip system for the ATLAS Phase-II upgrade [2], which is the subject of this case study, there are two additional temperature-dependent heat sources. The first is a radiation damage effect in the readout electronics, which leads to an increase in the digital power of the chip whose magnitude depends on the total ionisation dose (TID) and the temperature of the chip [2]. This phenomenon was first observed in the ATLAS IBL [3]. The other temperature dependence of a power source stems from the converter chip (FEAST [4]) used in the on-detector DC-DC converter system supplying power to the front-end electronics. The FEAST chip has an efficiency that decreases at higher temperatures; its efficiency also depends on the magnitude of the load current.

¹In a real detector system, the resulting growth of sensor temperature would be arrested by overcurrent limits in the power supplies, resulting in a reduction of the bias voltage. At the same time, the increased current leads to an increase of the noise, such that the overall result is a degradation of the S/N performance of the system.

31 In principle, the temperatures in the system for a given set of operational parameters (power density,
32 thermal conductivities, etc.) can be predicted using finite element analysis (FEA) to an accuracy that is
33 limited only by the quality of the input parameters. However, this is a time-consuming process and can be
34 prohibitively difficult if a number of local heat sources depend non-linearly on temperature. A simplification
35 to this problem that allows for an analytical solution in the case of a simple heat source topology has been
36 developed in [5]. Here we develop this method further to include several temperature-dependent non-linear
37 heat sources in the front-end electronics. The resulting set of equations cannot be solved analytically anymore,
38 but the solution can be found with little effort using numerical problem solvers. This enables us to predict
39 with some confidence the temperatures and power requirements in the ATLAS strip system throughout
40 Phase-II operation. The results from this prediction have been used throughout the ATLAS strip project to
41 consistently dimension the different systems (cooling, power, services, etc.), including an appropriate margin
42 due to the inclusion of a common set of safety factors. This method can be easily adapted to any other
43 system by adjusting the model to the system-specific geometries and parameters.

44 *1.1. The ATLAS strip system*

45 The strip system for the ATLAS Phase-II upgrade consists of two parts: the barrel system, comprised of
46 four concentric cylindrical barrels, and two endcaps consisting of six disks each.

47 The basic unit of the detector is the silicon-strip module. Modules are composed of sensors with hybrids
48 on top, which host the front-end chips as well as circuitry to convert the supply voltage to the chip voltages.
49 The modules are glued onto both sides of a composite sandwich (local support) that contains two parallel
50 thin-wall titanium cooling pipes embedded in carbon foam (Allcomp K9) between two facesheets of ultra-
51 high-modulus carbon fibre (3 layers of K13C2U/EX1515) co-cured together with a Kapton/copper low-mass
52 tape. During operation, cooling will be achieved by evaporating CO₂ in the cooling pipes with a final target
53 temperature no higher than −35°C anywhere along the local support.

54 In the barrel, the local support is called a stave, onto which 14 modules made with square sensors
55 (96.85 × 96.72 mm²) are loaded. Two types of module are used in the barrel: modules with ‘short-strip’
56 sensors of length 24.1 mm, and ‘long-strip’ sensor modules with 48.2 mm strip lengths. Short-strip modules
57 are used in the two innermost barrel layers, and long-strip modules in the two outermost barrel layers, mainly
58 for hit occupancy considerations. A model of the short-strip barrel stave geometry is shown in Fig. 1.

59 The geometry of the barrel stave is uniform along its length, with the exception of the end region of the
60 stave, where an End-Of-Substructure (EOS) card is mounted on both surfaces. The EOS card shares part of
61 its heat path with the adjacent module; underneath this module (hereafter referred to as an ‘EOS module’),
62 the thermal path is degraded by the presence of electrically-insulating ceramic pipe sections. The thermal
63 and electrical properties of an EOS module are sufficiently different from other modules along the length of
64 the stave (‘normal modules’) to warrant separate treatment in the thermo-electrical model of the barrel.

65 The endcap system consists of two endcaps composed of 6 disks each. Each disk contains 32 ‘petals,’ the
66 local substructure depicted in Fig. 2. Both sides of the petal are loaded with 6 modules, each with a distinct
67 design, located at increasing radius from the beam pipe and labelled R0 through R5 (where ‘R’ stands for
68 ring). Each endcap module consists of one or two wedge-shaped silicon sensors and a varying number of
69 front-end chips and DC-DC converters. The EOS card is located adjacent to the R5 module, but the cooling
70 pipes run directly underneath it without a shared heat path, in contrast to the barrel EOS card. Because
71 of the unique geometry of each module in a petal, each of the six different types of module is modelled
72 separately in the thermo-electrical model.

73 *1.2. Radiation environment*

74 A key input to the thermo-electrical calculation is the radiation environment of the strip system, as several
75 inputs depend on radiation damage effects. The sensor leakage current can be parametrized as a function
76 of the fluence expressed in 1 MeV neutron-equivalents, and the TID effect on the digital chip current will
77 be described as a function of the total ionizing dose rate (more details on its dependencies can be found in
78 Section 7).

79 Predictions for both of these quantities have been generated for each point in the ITk using the FLUKA
80 particle transport code and the PYTHIA8 event generator (Fig. 3) [6]. In the barrel system, both of these
81 distributions display a strong dependence on r but a weak z -dependence. Accordingly, we make the simplifying
82 assumption that modules within the same barrel layer have identical fluence and TID, and model four

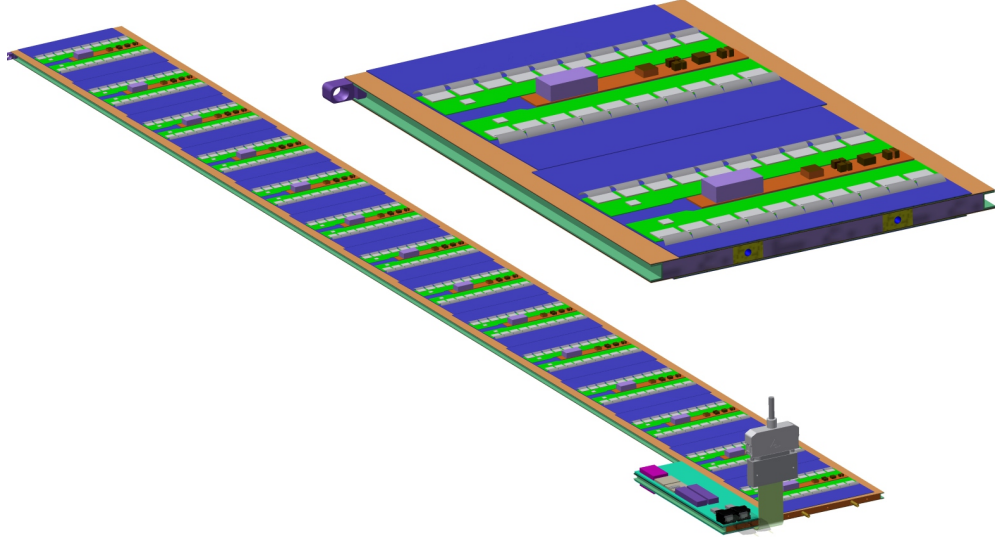


Figure 1: Strip barrel local support geometry. On the left, a complete stave is shown (EOS card in the foreground). The right picture shows a cross-section of the stave with the two cooling pipes visible inside the core.

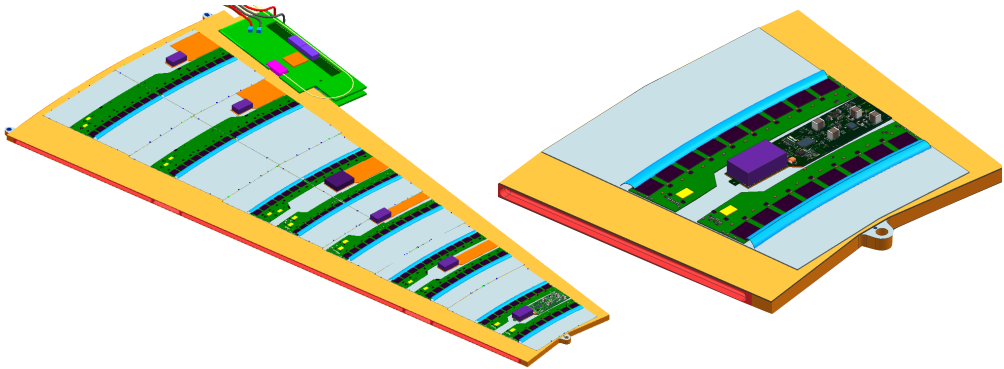


Figure 2: The geometry of the endcap strip petal, featuring 6 distinct module designs. A close-up of the R0 module is shown on the right.

83 different radiation profiles (one for each barrel layer). In the endcaps, the radiation levels vary significantly
 84 over the length of the petals and from disk to disk; therefore, we model each disk and ring position separately
 85 (36 in total).

86 2. The electrical model

87 The electrical model consists of low-voltage (LV) and high-voltage (HV) circuits, depicted in Fig. 4.
 88 The LV current (supplied at 11 V) is used to power the hybrid controller chips (HCCs) [2], ATLAS Binary
 89 Chips (ABCs) [7] and Autonomous Monitoring and Control chip (AMAC) located on PCBs that are glued
 90 directly onto the surface of the sensor. These chips require between 1.5 and 3.3 V, which are provided by the
 91 temperature-dependent FEAST DC-DC converter (labelled bPOL12V in Fig. 4) and an LDO (low-dropout)
 92 regulator (labelled linPOL12V). The number of chips and converters on each module vary according to the
 93 design of each different module type (barrel short-strip and long-strip modules, and six different endcap
 94 module designs). A barrel or endcap module contains 10–28 ABC chips, 1–4 HCCs, and 1–2 of each of the
 95 other components (linPOL12V/bPOL12V/AMAC).

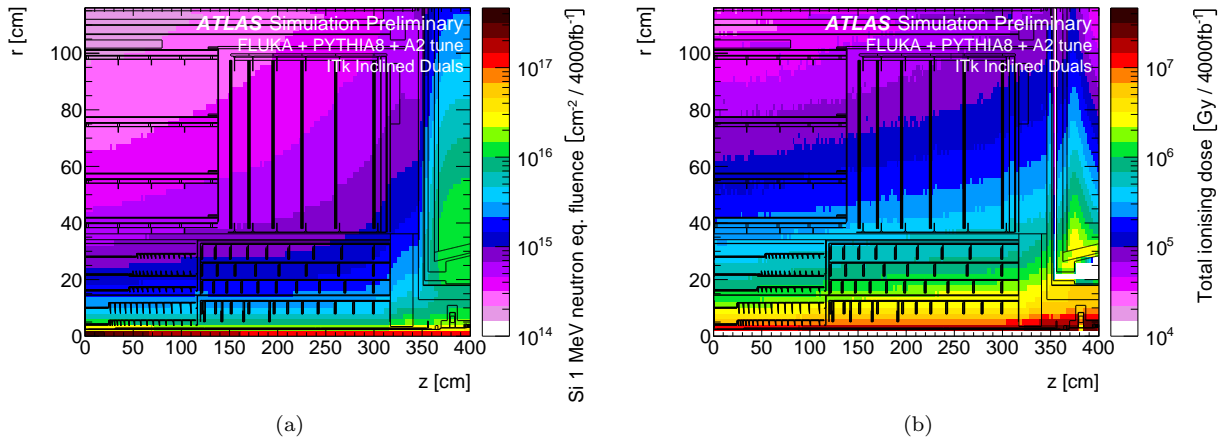


Figure 3: The ATLAS ITk radiation environment. (a) 1 MeV neutron equivalent fluence and (b) total ionizing dose. Both plots are for an integrated luminosity of 4000 fb^{-1} [6]. The figures use a rainbow colour gradient, with violet indicating the lowest values and red the highest values of fluence or ionizing dose.

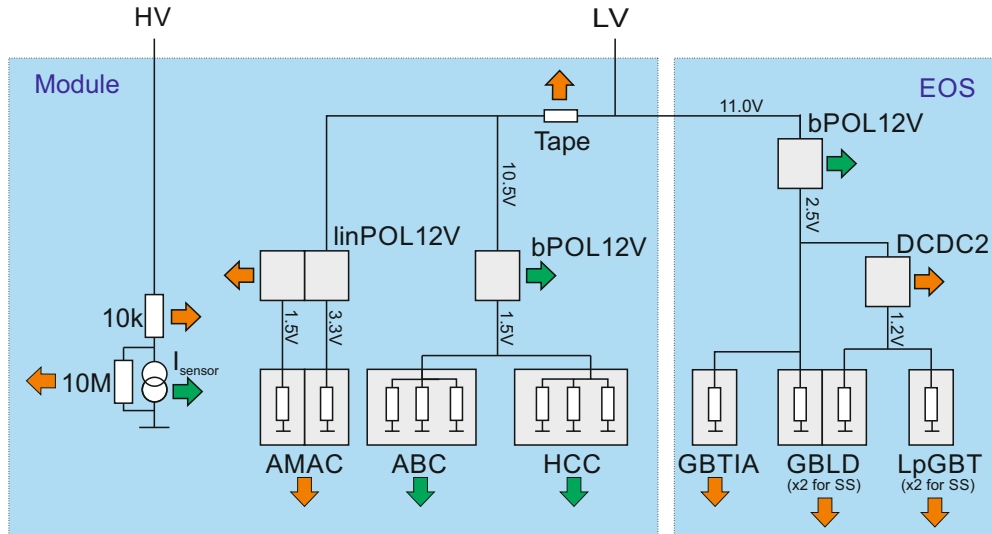


Figure 4: The electrical model of the ITk Strip barrel and endcap modules. Green arrows represent temperature-dependent heat sources, while orange arrows are temperature-independent. Grey squares are chips.

The LV current is also delivered to the EOS card to power various data transfer components: the Gigabit Laser Driver (GBLD), low power GigaBit Transceiver (LpGBT) and Gigabit Trans-impedance Amplifier (GBTIA) chips. A FEAST identical to the one used on the module is used to step the voltage down from 11 V to 2.5 V, and an additional DC-DC converter ('DCDC2') brings the voltage down further for some components. The short-strip barrel staves contain two GBLD and LpGBT chips.

The bus tape, which carries both LV and HV currents, has a small ohmic resistance, which impacts the module in two ways. First, the tape itself will generate some heat according to the amount of current passing through it; this source of heat is accounted for in the model, however the contribution to the total module power is negligible. Second, due to the voltage loss along the traces, there is a slight reduction in voltage supplied to successive modules along the substructure. The treatment of this effect is slightly different in the barrel and endcap models: in the barrel, the voltage delivered to every module is averaged to 10.5 V; in the endcap, the ΔV is estimated based on the calculated expected power loss along the tape for each module

108 and varies between 10.8 and 11 V. In both the barrel and endcap systems, the impact of using a different
 109 treatment is small.

110 Finally, the HV current provides the bias voltage on the silicon sensors. An HV multiplexer switch
 111 (HVMUX) can be used to disconnect the sensor from the bias line (it requires a $10\text{ M}\Omega$ resistor parallel to
 112 the sensor in order to function). Two HV filters with an effective resistance of $10\text{ k}\Omega$ are situated in series
 113 with the sensor. The nominal operating voltage of the sensor is expected to be 500V, but the system is
 114 designed to handle a bias voltage of up to 700V.

115 3. The thermal model

116 The thermal network consists of heat sources (some of which are temperature-dependent) and thermal
 117 resistances. The latter are given by the properties of the mechanical design (heat conductivities of the
 118 materials) and the geometry of the heat path. The geometry is generally 3-dimensional, but it is the strategy
 119 of the simple network models to lump the 3D behaviour into one thermal resistance parameter. In the models
 120 discussed here, we have used a granularity corresponding to single detector modules for which the thermal
 121 resistance has been modelled. The temperatures in the model are then given for the nodes in the network in
 122 analogy to the potentials in an electrical network.

123 The complexity of the thermal network used in this study, depicted in Fig. 5, is given by the variety of
 124 temperature-dependent heat sources in the ATLAS strip system: the digital power for each type of chip, the
 125 FEAST chip providing the on-detector DC-DC conversion, and the sensor leakage power. In the ATLAS
 126 ITk strip modules, all of these components are located on top of the sensors, such that the heat generated
 127 in them flows through the sensor into the support structure, the stave (barrel) or petal (endcap) core with
 128 the embedded cooling pipe. In the network model, the heat flow from these sources combines and travels
 129 through a common impedance R_M to the sink at a temperature T_c . For each of the temperature-dependent
 130 heat sources (ABC, HCC, FEAST and the sensor) we have added a resistance from the common temperature
 131 T_{mod} to allow for a finite and different heat path for each of them. Finally, the EOS card adjacent to the last
 132 module on the barrel stave or endcap petal is modeled as an additional source of heat with an independent
 133 impedance for its unique thermal path.

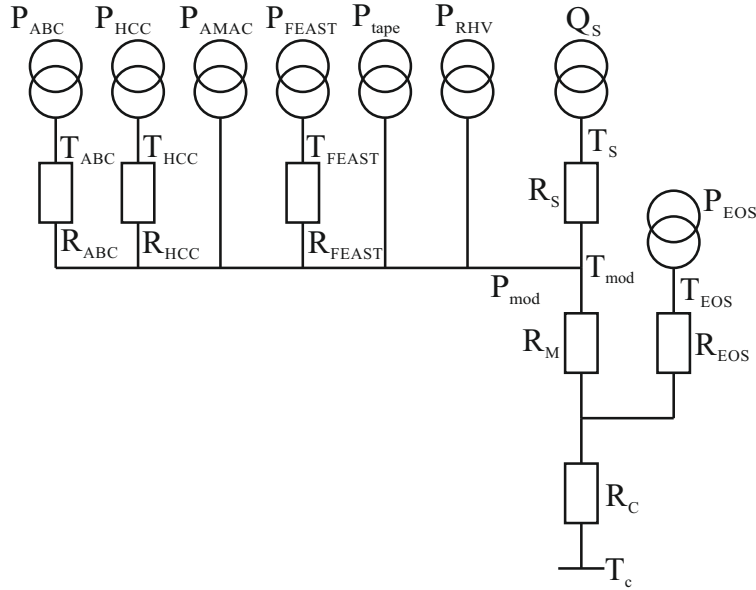


Figure 5: Thermal network model.

134 This is a more complex thermal network than the one studied in Ref. [5], for which an analytical solution
 135 for the determination of thermal stability is given. In particular, because of the non-linear temperature
 136 dependence of some of the heat sources, it is not possible in the present case to solve the set of equations

137 describing the model analytically. However, the set of equations is still sufficiently small to solve numerically
138 using any modern programming language.

139 4. Obtaining thermal impedances using FEA

140 The cooling path between the sources dissipating electrical power and the cooling fluid is 3-dimensional
141 and includes components with orthotropic thermal conductivity. Hence the prediction of temperature at any
142 node of the model requires a 3D thermal FEA [8, 9]. However, the thermal conductivities of the components
143 along the path are approximately constant, so that the temperature rise ΔT_i above the coolant temperature
144 of any node i ($i = \text{ABC, HCC, AMAC, FEAST, tape, RHV, or sensor}$) in the thermal network model is
145 adequately described by a linear sum of contributions from individual sources, i.e:

$$\Delta T_i \equiv T_i - T_C = R_i P_i + (R_C + R_M) \sum_j P_j, \quad (2)$$

146 where the index j runs over all powered nodes. (We have momentarily ignored the contribution from the
147 EOS card.)

148 In order to extract the thermal impedances for the thermal network model, the finite element model is run
149 multiple times, with each heat source (or group of similar sources) switched on in turn with a representative
150 amount of heat. In each of these cases, the temperature is calculated for all nodes in the thermal network
151 model (Fig. 5). The temperature of a node is here taken as the average of the temperatures for all the
152 grid points in the FEA model within the volume of the object corresponding to the node². The thermal
153 impedances are then obtained from a fit of Eq. 2 using the temperature data for all nodes for all cases of
154 heat injection.

155 Because of the nature of the network, the fitted value for the common impedance $R_{CM} = R_C + R_M$ is
156 determined by the observed temperature rises of components where no heat is injected. The linearity of
157 this relationship is illustrated in Fig. 6. The value of each component-specific impedance is determined from
158 the temperature rise observed when heat is injected into that component. The linear approximation of the
159 model reasonably describes the FEA simulation, and the level of disagreement, discussed below, is taken as
160 an uncertainty that is assessed as a safety factor as described in Section 7.2.

161 For the barrel, this procedure is performed for both an EOS module and a normal module, for short-
162 strip and long-strip module types and for 6 different heat sources (24 module FEA simulations in total).
163 In all cases, the agreement of the network temperatures using the thermal impedances from the fit with
164 the data from FEA is better than 0.5°C for all nodes. The thermal impedance from the sensor to the sink
165 (R_{CM}) is consistently between 1.1 and 1.4 °C/W, but higher values (between 10 and 20 °C/W) are found
166 for other impedances in the network (R_{HCC} and R_{FEAST}), mostly because these are for components with a
167 small footprint constituting a bottleneck for the heat flow. A 10% uncertainty is assigned to the thermal
168 impedances in the barrel modules for the purposes of assessing safety factors.

169 For the endcap, the procedure to determine the thermal impedances for each of the 6 module types used
170 simulations of an endcap petal with 3 different heat sources (requiring 3 FEA simulations of a full petal).
171 R_{CM} ranges from 0.6 to 1.4 °C/W, with other nodes between 5 and 20 °C/W. Because the location of powered
172 components is more irregular on an endcap module, the difference between the predicted temperatures of the
173 linear network and the FEA can reach up to 1.2 °C for key temperature-dependent nodes. Therefore, a 20%
174 uncertainty is assigned to the thermal impedances in the endcap modules.

175 There are two recognised departures from linearity of the thermal path: the rise in thermal conductivity
176 of the silicon sensor with decreasing temperature, and the rise in heat transfer coefficient (HTC) of the
177 evaporating CO₂ coolant with increasing thermal flux. The FEA models are run using mean values for these
178 quantities appropriate to the operating conditions, and the thermo-electrical model results are insensitive to
179 the variations expected in practice. However, if this level of realism is required and if reliable parametrizations
180 for these dependencies can be obtained, then the inclusion of such variations in the model is possible.

2This is particularly interesting in the case of the sensor, which fills a large volume, with a potentially large range of temperatures. In Ref. [5] the analytic model parameters were extracted from the maximum sensor temperature predicted by FEA, whereas our subsequent studies have shown that the thermal stability limit is predicted more accurately if the average sensor temperature is used.

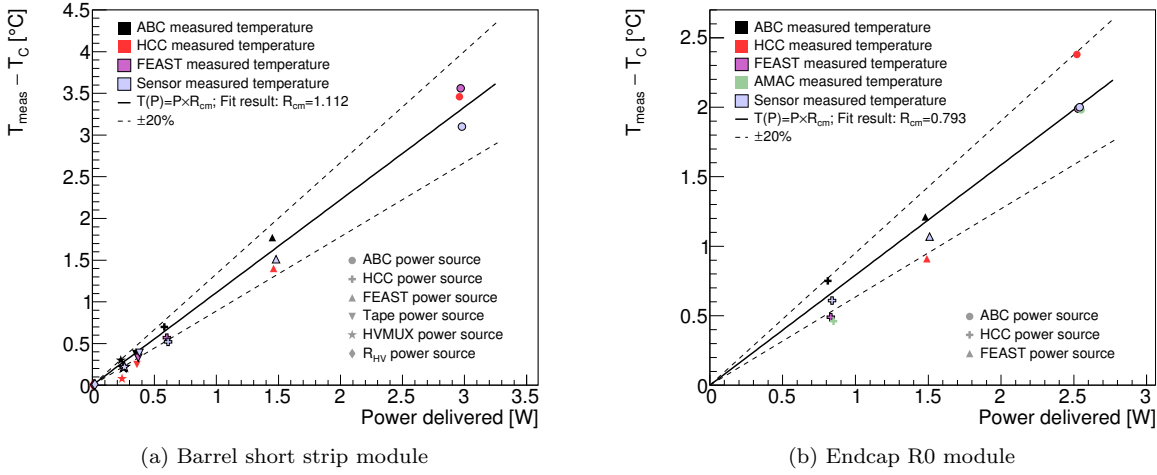


Figure 6: The relationship between the temperature rise observed in the FEA for a specific component and the heat injected in another component. The slope of the fitted line is the estimate for R_{CM} . (a) The fit for a short-strip barrel module adjacent to the EOS card. (b) The fit for the endcap R0 module. For each data point marker, the source of power is indicated by the shape, and the measured component is indicated by the colour (black: ABC, red: HCC, magenta: FEAST, green: AMAC, light blue: silicon sensor). The dashed lines represent a $\pm 20\%$ error band on the fit for R_{CM} .

181 5. Other model inputs

182 The three temperature-dependent elements of the thermo-electrical model—the radiation-induced digital
 183 current increase in the front-end chips, the efficiency of the FEAST-controlled DC-DC converter, and the
 184 sensor leakage current—are described in this section. Each effect is studied experimentally and fit with
 185 functional forms in order to accurately represent them in the model. The uncertainty in the experimental
 186 data, and in our modelling assumptions, are estimated here and considered in the evaluation of safety factors,
 187 described in detail in Section 7.2.

188 5.1. DC-DC converter

189 The DC-DC converter, controlled by the FEAST chip, supplies a low-voltage (1.5 V) current to the
 190 ABC130 and HCC front-end chips on the module. The efficiency of the FEAST depends on its temperature
 191 as well as the output (load) current load delivered to the front-end chips. To correctly model the FEAST
 192 efficiency, experimental measurements have been performed to characterize the dependence and fitted with
 193 a functional form.

194 For the measurement, the FEAST power board was glued to an aluminum cold plate, cooled with CO₂,
 195 and powered with the nominal working input and output voltages (11 V input, 1.5 V output). The temper-
 196 ature of the FEAST was measured with an NTC (negative temperature coefficient) thermistor and a PTAT
 197 (proportional to absolute temperature) sensor residing on the FEAST for a range of load currents up to the
 198 maximum design current of 4A.

199 The data was then fit with a function with sufficient parameters to ensure reasonable agreement; the
 200 choice of functional form has no physical interpretation. Fig. 7 depicts the FEAST efficiency data and the
 201 parametrized fit used in the model. The parametrization fits the data with an accuracy better than 1%;
 202 this uncertainty in the FEAST efficiency modelling is small compared to other uncertainty sources, and is
 203 therefore neglected in our model.

204 5.2. Digital current increase of chips using 130 nm CMOS technology

205 The ABC and HCC chips, designed using IBM 130 nm CMOS 8RF technology, are known to suffer from
 206 an increase in digital current when subjected to a high-radiation environment [2]. This phenomenon, known

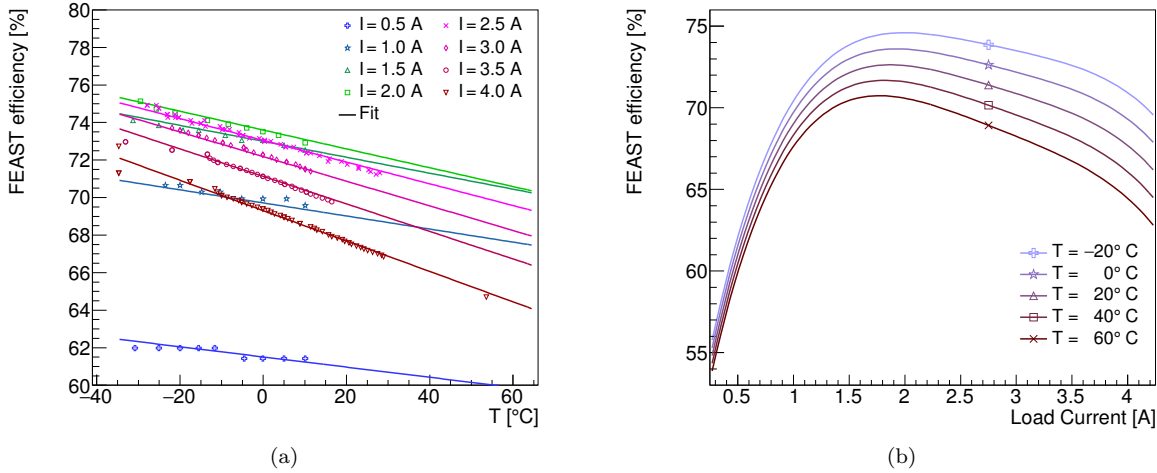


Figure 7: The FEAST efficiency model based on experimental data. (a) The experimental data points characterizing the FEAST efficiency are plotted as markers and coded by colour and marker style for load current. The data is compared to the analytic fit, evaluated in curves of equal current. (b) The same analytic fit, presented as a function of current load for curves of equal temperature.

as the ‘‘TID bump,’’ is well-studied [10, 11] and has a characteristic shape whereby the effect reaches a maximum as a function of the accumulated dose and then gradually diminishes (see Fig. 8).

In an effort to characterize the nature of the TID bump in the ABC and HCC chips empirically, many irradiation campaigns have been conducted using a variety of radiation sources, testing the effect at different temperatures and dose rates. The data collected from these studies was used to develop a model of the TID bump that estimates the digital current increase given the total ionizing dose, the dose rate, and the operating temperature of the chip. This parametrization, which is depicted in Fig 8, is used as an input to the thermo-electrical model in order to correctly model the ABC and HCC currents. The TID bump is assumed to fully apply to the HCC digital current, and apply to 69% of the ABC digital current (according to our understanding of its digital circuitry).

The TID bump displays certain key features, which are reflected in the parametrization: first, the effect is larger at colder temperatures and higher dose rates. This means it can be mitigated by operating the chips at higher temperature (note that the dose rate is determined by the LHC operational conditions). Second, the figure illustrates how chips receiving different dose rates will reach their maximum digital current increase at different times. This feature is particularly important when modelling the total power consumed by the barrel and endcap systems. In both systems, the dose rate varies significantly depending on the position of the module in the detector. The effect means that the maximum system power will be smaller than the sum of the maximum power of each module, as each chip reaches its maximum at a different point in time (see Section 7.4).

The TID bump is an important source of uncertainty in our model. The experimental data exhibit a relatively large variation in the TID bump effect, in particular between different batches of the same type of chip delivered by the manufacturer, suggesting an unknown effect in the fabrication process. To estimate the uncertainty in the TID bump, the parametrized function is fit again using only the worst-performing data (defined as having the largest TID bump effect). This ‘‘pessimistic’’ parametrization is used as a safety factor to estimate the detector performance in worst-case scenarios.

The irradiation of individual chips have typically been performed at constant dose rate and temperature. However, both of these parameters will vary as a function of time in the scenarios that we attempt to model. In our current parametrization, we use only the instantaneous value of these two parameters, thus neglecting any possible history of the TID effect for a given chip. We also ignore any short-term effects due to variations in the dose rate on the scale of hours or days. This approach is mandated by the lack of more varied experimental data and the absence of a good theoretical model for this effect. This probably constitutes the largest source of uncertainty in our model.

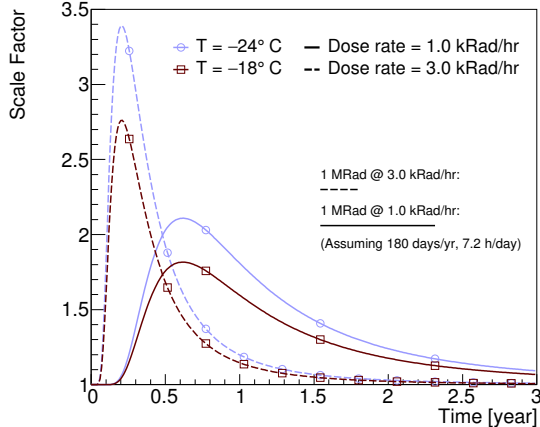


Figure 8: Parameterization of the impact of ionizing radiation on the magnitude of the front-end chip digital current (the TID bump), presented as a function of time elapsed during detector operation. The current is multiplied by a scale factor that is modeled as a function of total ionizing dose, dose rate, and temperature, using a fit to experimental data. The figure presents four scenarios using two different chip temperatures and dose rates. The relationship between time and total ionizing dose is calculated assuming the detector operates for 180 days per year, 7.2 hours per day. The time that it takes to reach 1 MRad of total ionizing radiation is indicated on the figure for both dose rates.

239 **5.3. Radiation-dependent leakage current**

240 The radiation-induced sensor leakage current can be parametrized as a function of the hadron fluence
 241 expressed in 1 MeV equivalent neutrons. We have used linear parametrizations obtained from fits to ex-
 242 perimental data taken at 500 V and 700 V at -15°C , and scale them to a given sensor temperature using
 243 Eq. 1.

244 **6. Running the model**

245 The thermo-electrical model constructs a profile of the sensor module operation conditions over the
 246 lifetime of the detector in the following manner. First, the total module power (including all components,
 247 but excluding the sensor leakage power) and the sensor temperature assuming no leakage current (T_0) are
 248 calculated using a reasonable set of initial component temperatures. The initial value for the module power is
 249 used to solve for the sensor power and temperature accounting for leakage current, using the thermal balance
 250 equation and the relationship from Eq. 1. Using this calculated sensor leakage current and temperature, the
 251 power and temperature of the module components are updated given the initial (year 0, month 0) startup
 252 parameters.

253 Next, the module conditions of the following month (year 0, month 1) are calculated. Using the compo-
 254 nent temperatures calculated from the previous month and the operational parameters (ionizing dose and
 255 dose rates) from the current month, the module total power (excluding sensor leakage) is again calculated,
 256 and subsequently the sensor temperature and leakage current are computed. Following this, the module
 257 component temperatures and power values are derived for this month. This process is repeated in one-month
 258 steps until the final year of operation, or until a real solution for the sensor temperature does not exist,
 259 indicating that thermal runaway conditions have been reached.

260 In the barrel subsystem, the above procedure is performed four separate times to represent the radiation
 261 conditions of the four barrel layers located at different radii from the beam axis³ for both a normal and an
 262 EOS-type module. Thus, eight modules are simulated in total for the barrel (4 layers \times normal/EOS), and
 263 they are combined in their proper proportion to simulate the entire barrel system.

³The correct module type, short-strip in the inner two layers and long-strip for the outer two layers, is used for each layer.

264 In the endcap subsystem, the total ionizing dose and dose rates vary significantly depending on the
 265 position of the module; furthermore, the design of each module on a petal differs significantly. Therefore, all
 266 36 module types (6 rings \times 6 disks) are simulated independently, and combined to represent the full endcap.

267 We have implemented this algorithm separately for the barrel and endcaps. In both cases, the calculation
 268 for a set of operating conditions over the full lifetime of the LHC, in steps of one month, takes between 5
 269 and 10 minutes on a standard PC. The results represent the equivalent of simulating 1152 barrel modules
 270 and 5184 endcap modules⁴. For comparison, a single steady-state FEA simulation of an endcap petal takes
 271 about 20 minutes. Thus, the thermo-electrical model enables a quick turn-around for systematic studies of
 272 the parameter space that would not be possible using FEA alone.

273 7. Outputs of the thermo-electrical model

274 The thermo-electrical model provides a wide range of predictions for the operation of the strip system. A
 275 detailed discussion of all results is beyond the scope of this article; instead, we present here a subset of the
 276 results to demonstrate the capabilities and use of the thermo-electrical model for the design of the detector
 277 system.

278 7.1. Operational scenarios

279 To study the different aspects of our predictions for the operation of the ITk strip system throughout
 280 its lifetime, we performed the calculation of the system parameters over the expected 14 years of operation
 281 in monthly steps as outlined in Section 6. Time-dependent operational inputs to the calculation were taken
 282 from the expected performance of the HL-LHC (Fig. 9a). For the cooling, which can be adjusted during data
 283 taking using detector control systems, we studied flat (constant) coolant temperature profiles ranging from
 284 from 0°C to -35°C, the lowest evaporation temperature achievable with the ITk evaporative CO₂ cooling
 285 system. We also studied a ‘ramp’ scenario in which the coolant temperature starts at 0°C and is gradually
 286 lowered down to -35°C over the course of 10 years (Fig. 9b).

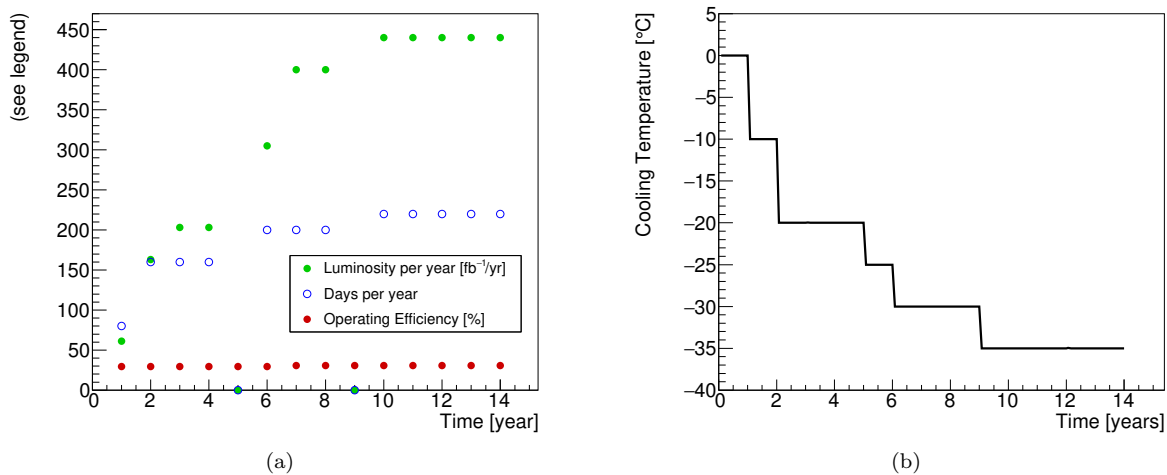


Figure 9: (a) Expected HL-LHC performance and (b) ‘cooling ramp’ scenario for the coolant temperature. Year-long shutdowns of the LHC are anticipated in years 5 and 9.

⁴Recall from Section 4 that the thermo-electrical model requires FEA simulations of 24 barrel modules and 3 endcap petals to extract the thermal impedances, but this procedure is only performed once.

287 *7.2. Safety factors*

288 To ensure the robustness of the system design against uncertainties in the assumptions used in the model,
 289 we also evaluate the model using a set of input parameters with some key inputs degraded. The set of safety
 290 factors used is given in Table 1. Each safety factor has been estimated individually based on experience, the
 291 complexity of the system aspect described by the parameter, and from available data or the absence of such
 292 data. Note that the model can be evaluated with all the safety factors listed in Table 1 used together, a
 293 situation that is unlikely to occur in the real system, to provide a worst-case estimate for the performance of
 294 the ITk strip system. The individual effects of the different safety factors are demonstrated in Fig. 10.

Table 1: Safety factors.

Safety factor	Value	Reason
Fluence	50%	Accuracy of fluence calculations and uncertainties in material distributions
Thermal impedance	10% barrel, 20% endcap	Local support build tolerances, thermal network assumptions
Digital current	20%	Final chip performance and parametrization of TID effect
Analog current	5%	Final chip performance
Tape electrical impedance	10%	Electrical tape manufacturing tolerances
Bias voltage	700 V	Increased bias voltage from nominal 500 V to maintain S/N
TID parametrization	Nominal/Pessimistic	Different data sets for fit of TID bump

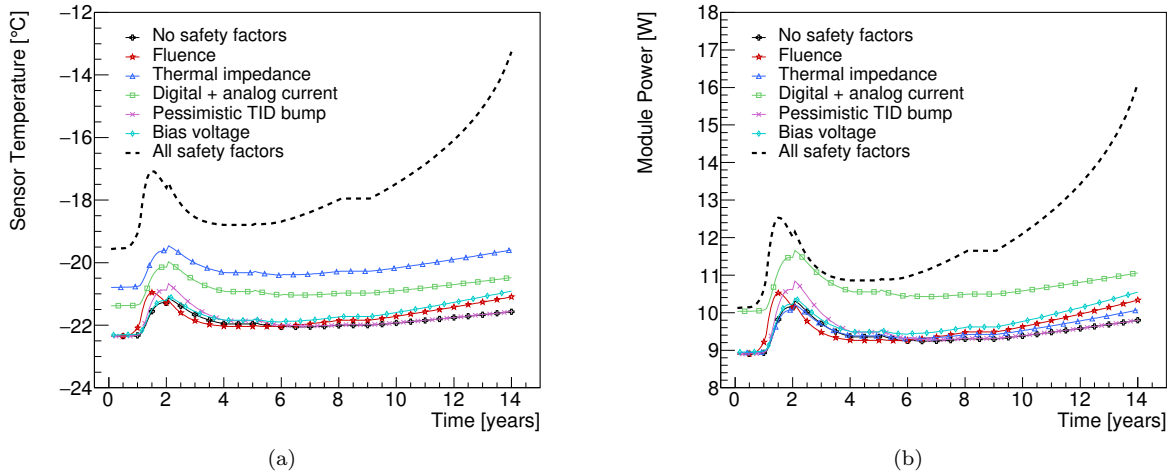


Figure 10: Comparing the impact of different safety factors on (a) the sensor temperature and (b) the module power for the endcap R3-type module, using a flat cooling scenario (-30°C). The dotted line depicts the effect of all safety factors applied at once.

295 It is important to note that combining multiple safety factors can have a compounding effect on the
 296 system. As an example, the effect of an increased bias voltage combined with a larger digital current will
 297 result in a much higher sensor leakage current at the detector end-of-life than either situation occurring
 298 individually. The analytical model presented here allows for scenarios like these to be examined quickly and
 299 effectively.

300 *7.3. Module properties*

301 Several module properties predicted by the thermo-electrical model are shown in Figs. 11 and 12 for
 302 the barrel system. The different radiation-dependent effects occur on different timescales. The maximum
 303 in the digital chip power due to the TID effect occurs relatively early (in year 1 to 4), although the bump

304 has a long tail, particularly in the outer layers of the barrel. The sensor leakage power, on the other hand,
 305 grows towards the end of the lifetime of the ITk. If the leakage current continued to increase in the case of
 306 further irradiation, or if the cooling temperature were raised, this growth would ultimately lead to thermal
 307 runaway. Due to the radial dependence of the radiation environment, the radiation-induced effects are most
 308 pronounced in the innermost barrel layers.

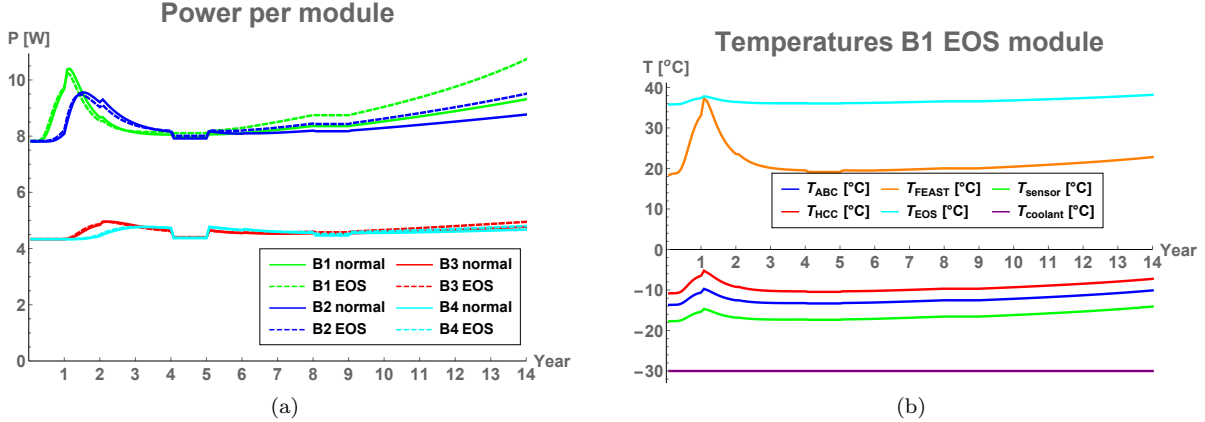


Figure 11: Examples of barrel module performance predictions for a flat cooling scenario (-30°C) including safety factors. (a) Power per module. (b) Temperatures for different nodes of an end-of-stave barrel module in the innermost barrel. The discontinuities in year 5 and 9 are due to anticipated year-long shutdowns of the LHC.

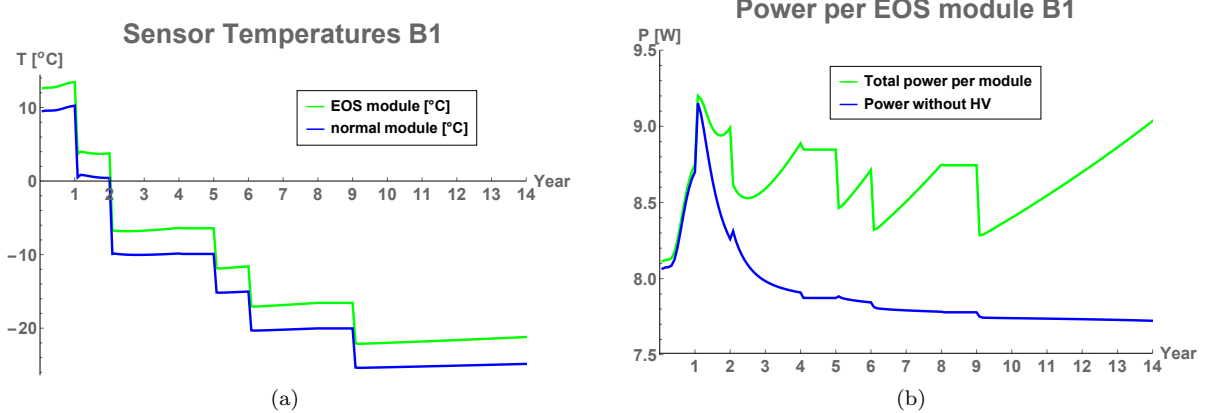


Figure 12: Examples of barrel module performance predictions for the ramp cooling scenario including safety factors. (a) Sensor temperature in the innermost barrel modules. (b) Power in an end-of-stave barrel module in the innermost layer.

309 7.4. System properties

310 One of the key concerns for the design of the strip system is thermal stability of the system. If the
 311 cooling temperature is too high to limit the leakage power from the radiation-damaged sensors to a level
 312 where the heat can still be removed, the system is unstable (it goes into ‘thermal runaway’). To find the
 313 cooling temperature T_C at which this condition is reached, we make repeated simulations of the ITk strip
 314 system using the thermo-electrical model, with each simulation representing the full 14-year operation of
 315 the ITk at a fixed T_C . Between simulations, T_C is increased in steps of 5°C until the model finds thermal
 316 runaway. In the numeric evaluation of the thermo-electrical model this manifests itself in the absence of a

317 solution to the system of equations. In the endcap strip system, this occurs at a cooling temperature of
 318 -15°C under nominal conditions (i.e. with no safety factors applied); in this scenario, thermal runaway
 319 would be reached in the 12th year of operation. With all safety factors applied, thermal runaway would occur
 320 at a cooling temperature of -25°C (in year 10). In the barrel system, where the radiation environment is
 321 slightly less intense, the conditions for thermal runaway occur at the same cooling temperatures, but a few
 322 years later than in the endcaps: in the final year of operation and a cooling temperature of -15°C under
 323 nominal conditions, and at -25°C (in year 13) with safety factors applied. As the design cooling temperature
 324 of the ITk cooling system is -35°C , we have confidence that the ITk strip system has a sufficient margin for
 325 thermal stability.

326 Beyond the issue of stability, the thermo-electrical model delivers predictions for the development of
 327 current and power requirements for the overall system. Some of the predictions are shown in Fig. 13. Again,
 328 the different timescales of the various radiation-induced effects are visible; ignoring this time dependence
 329 could lead to over-specification of some system aspects. Taking Fig. 13b as an example, the average module
 330 power (indicated by the thick black line) is 6.6 W in the beginning of operation and reaches 8.0 W at the TID
 331 bump, in the second year. If we naively summed the maxima of the TID bumps, neglecting time dependence,
 332 we would arrive at 8.6 W, overestimating the power at the TID bump by 7.5% and overestimating the effect
 333 of the TID bump by 43%. The difference, multiplied in the endcap by 4608 modules, amounts to nearly
 334 3 kW of power and impacts the specifications of e.g. the cooling system.

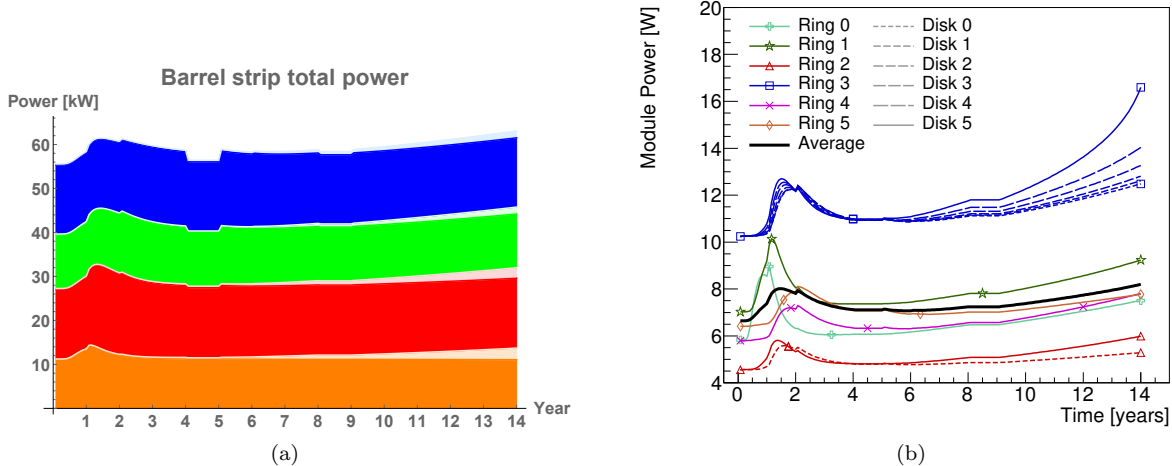


Figure 13: Examples of system performance predictions. (a) Barrel total power requirements. The plot shows the stacked power requirements for the four barrel layers (purple: layer 1, orange: layer 2, red: layer 3 blue: layer 4). Full colour indicates power from the front-end electronics, and hatched parts are contributions from HV power for the four barrels. The discontinuities in year 5 and 9 are due to anticipated year-long shutdowns of the LHC. (b) The power requirements for 12 of the 36 simulated endcap modules, labelled according to their ring type and disk position. (Modules are omitted to improve the clarity of the figure.) The solid black line indicates the average module power. Both predictions use a scenario with flat -30°C cooling and including all safety factors.

335 The predictions from this model are now used throughout the strip project to consistently size the power
 336 supply and cooling systems. Including safety factors in the predictions gives us some confidence that the
 337 designs are robust; by using commonly agreed safety factors, we ensure a consistent use of safety factors
 338 throughout the project and prevent safety factor creep.

339 Because of the different timescales for the peak power due to the TID effect and the radiation-induced
 340 sensor leakage, there is room to optimize the cooling temperature profile to minimize the total power in the
 341 strip system while avoiding thermal runaway. The thermo-electrical model is a powerful tool to plan such an
 342 optimized cooling profile. In fact, the cooling ‘ramp’ scenario introduced in Section 7.1 is the result of such
 343 an optimization. In this scenario, depicted in Fig. 14, the cooling temperature begins at a relatively high
 344 value (0°C) to minimize the impact of the TID bump in the first two years of operation, thus avoiding a

³⁴⁵ peak in the module power (see Fig. 14a). In subsequent years, T_C is steadily decreased to maintain a sensor
³⁴⁶ current at or below about 1 mA, as illustrated in Fig. 14b, in the interest of both minimizing the module
³⁴⁷ power and avoiding thermal runaway.

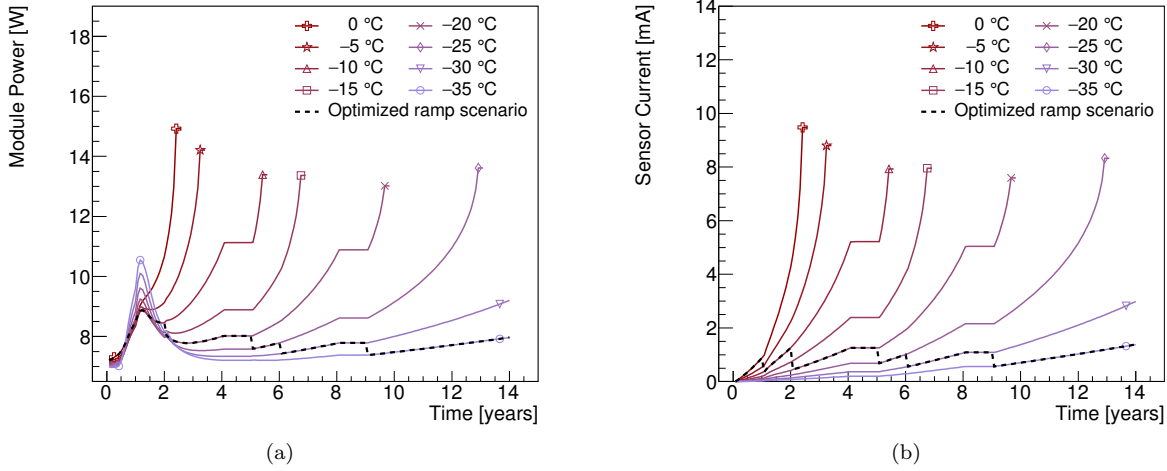


Figure 14: (a) Total power and (b) sensor leakage current of the endcap R1-type module for eight different flat cooling profiles, ranging from 0°C to -35°C , as well as the cooling ramp scenario specified in Fig. 9b (dashed curve). The curves that are discontinued before year 14 correspond to scenarios that have reached thermal runaway. The cooling ramp scenario has been selected to minimize the module power while keeping the sensor leakage current stable throughout the lifetime of the ITk. All safety factors are applied in these plots.

³⁴⁸ 8. Model performance verification

³⁴⁹ The accuracy of the predictions of the thermo-electrical model is affected by two major factors: the quality
³⁵⁰ of the input parameters, and the error introduced by reducing the complex 3D geometry into a linear thermal
³⁵¹ impedance network. The former has been discussed throughout this paper where the different inputs have
³⁵² been presented. For the latter, we have studied the agreement of predictions from the network model with
³⁵³ the more accurate results obtained from FEA for selected states of the system.

³⁵⁴ To verify the level of this agreement, we have calculated the sensor temperature curve for a barrel EOS-
³⁵⁵ type module up to thermal runaway, both in the full FEA and in the network model. For this exercise, we do
³⁵⁶ not vary any of the input parameters in the model other than the sensor leakage power with its temperature
³⁵⁷ dependence. The resistor values in the network model are the same as used throughout for our model,
³⁵⁸ obtained as described in Section 4. For the power from the various electronics components, the FEAST
³⁵⁹ efficiency and the TID scale factor we have used representative nominal values.

³⁶⁰ Because the variable model inputs are kept constant for this study, we can reduce the complex thermal
³⁶¹ network to its Thévenin equivalent, which is identical to the network studied in Ref. [5], and use the analytical
³⁶² expressions given there. The reduced network is described by the base temperature T_0 , defined as the sum
³⁶³ of the coolant temperature and the temperature rise due to the front-end electronics alone, and the total
³⁶⁴ thermal impedance R_t from the sensor to the coolant. Using the nominal resistances and representative power
³⁶⁵ numbers from the module, $T_0 = -21.9^{\circ}\text{C}$ and $R_t = 1.132 \text{ K/W}$ in the network model, compared to -22.4°C
³⁶⁶ and 1.147 K/W obtained directly from the FEA. The comparison of the predicted sensor temperatures for
³⁶⁷ both cases is shown in Fig. 15. Despite a large temperature variation of about 10°C across the sensor,
³⁶⁸ the network model runaway prediction agrees well with the FEA⁵. This gives us confidence that the use

⁵The critical temperature here is -12.4°C , which is higher than the numbers given in Section 7.4, because the study here ignores temperature effects such as the FEAST efficiency, which can only be modelled in the network model.

369 of a thermal network model is not likely to significantly degrade the predictions beyond the uncertainties
 370 introduced by other inputs to the model.

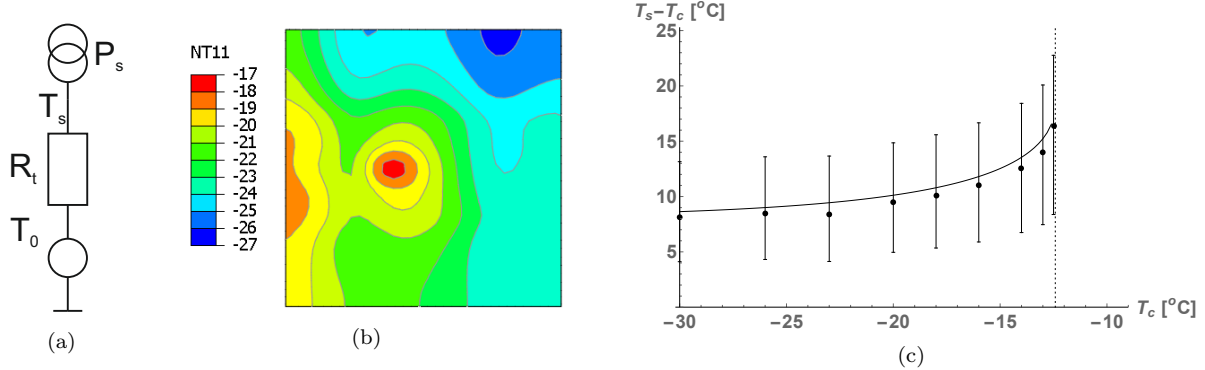


Figure 15: (a) Thévenin equivalent of the thermal network. (b) Result of sensor surface temperature calculations using FEA, assuming zero sensor power. The EOS card is to the left of the module, and the cooling pipes run from top to bottom about a quarter of the module width from each edge. The figure uses a rainbow colour gradient, with violet indicating the lowest temperatures and red the highest temperatures. (c) Difference of average sensor and coolant temperature, comparing FEA (red points) and the network model prediction (blue curve). The bars on the FEA data indicate minimum and maximum sensor temperature. The dotted vertical line indicates the critical temperature derived analytically using the network model (-12.4 °C).

371 9. Conclusions

372 We have developed a model of the ATLAS ITk strip system that is based on the interplay between a
 373 thermal and an electrical network model. The set of equations in the model can be numerically solved using
 374 standard data analysis software in a short time, allowing for a quick turn-around for systematic studies of the
 375 system performance. The complexity of these networks is given by the number of interconnected components
 376 between the networks, many of which have a non-linear dependence on the temperature or electrical power.
 377 This approach can be easily adopted for any other silicon detector system.

378 In the case of the ATLAS strip system, several temperature-dependent heat sources had to be modeled.
 379 In addition to the sensor leakage current, these are the radiation-induced increase of the digital front-end
 380 power ('TID bump') and the efficiency of the DC-DC conversion system. The outputs of the model give
 381 us confidence that the ITk strip system will be thermally stable until the end of LHC Phase-II operation,
 382 even with the inclusion of safety factors on key inputs. Furthermore, the model provides information for
 383 benchmark system parameters like cooling, supply power and currents in power cables, which is used in the
 384 specification of these systems. The use of the model outputs throughout the strip project ensures consistent
 385 specifications, including a common strategy on safety factors. Using the thermo-electrical model, we can also
 386 propose an optimized cooling temperature 'ramp' scenario, which stabilizes leakage power throughout the
 387 lifetime of the experiment while minimizing the TID bump.

388 We have verified the performance of the thermal network model compared to a full FEA treatment, and we
 389 are confident that the level of disagreement is smaller than the uncertainty introduced by the model inputs.
 390 Among the inputs, the most likely source of uncertainty stems from the limitations in our understanding of
 391 the parametrization of the TID effect.

392 10. Acknowledgements

393 The evaluation of the thermo-electrical model depends critically on the input parameters to the model.
 394 To capture the whole of the system, these need to distill all that is known of the system, and we are therefore
 395 indebted to the whole of the ITk strip community. In particular, we would like to thank Tony Affolder, Kyle

³⁹⁶ Cormier, Ian Dawson, Sergio Diez Cornell, Laura Gonella, Ashley Greenall, Alex Grillo, Paul Keener, Steve
³⁹⁷ McMahon, Paul Miyagawa, Craig Sawyer, Francis Ward and Tony Weidberg for all their inputs to this work.
³⁹⁸ The research was supported and financed in part by the UK's Science and Technology Facilities Council
³⁹⁹ and the Helmholtz Association (HGF) in Germany.

⁴⁰⁰ **References**

- [1] A. Chilingarov, Temperature dependence of the current generated in Si bulk, Journal of Instrumentation 8 (10) (2013) P10003–P10003. doi:10.1088/1748-0221/8/10/p10003.
URL <https://doi.org/10.1088%2F1748-0221%2F8%2F10%2Fp10003>
- [2] A. Collaboration, Technical Design Report for the ATLAS Inner Tracker Strip Detector, Tech. Rep. CERN-LHCC-2017-005, ATLAS-TDR-025, CERN, Geneva (Apr 2017).
URL <https://cds.cern.ch/record/2257755>
- [3] Radiation induced effects in the ATLAS Insertable B-Layer readout chip, Tech. Rep. ATL-INDET-PUB-2017-001, CERN, Geneva (Nov 2017).
URL <https://cds.cern.ch/record/2291800>
- [4] A. Affolder, B. Allongue, G. Blanchot, F. Faccio, C. Fuentes, A. Greenall, S. Michelis, DC-DC converters with reduced mass for trackers at the HL-LHC, Journal of Instrumentation 6 (11) (2011) C11035.
URL <http://stacks.iop.org/1748-0221/6/i=11/a=C11035>
- [5] G. Beck, G. Viehhauser, Analytic model of thermal runaway in silicon detectors, Nucl. Instrum. Meth. A618 (2010) 131–138. doi:10.1016/j.nima.2010.02.264.
- [6] Atlas experiment - radiation simulation public results [cited 2018-11-17].
URL https://twiki.cern.ch/twiki/bin/view/AtlasPublic/RadiationSimulationPublicResults#FLUKA_Simulations
- [7] N. Lehmann, Tracking with self-seeded Trigger for High Luminosity LHC, Master's thesis, Section of Electrical and Electronical Engineering, École Polytechnique Fédérale de Lausanne, Lausanne Switzerland (2014).
URL https://documents.epfl.ch/users/n.nl/nlehmann/www/SelfSeededTrigger_MasterThesis/SelfSeededTrigger_NiklausLehmann_Thesis.pdf
- [8] M. Smith, ABAQUS/Standard User's Manual, Version 6.9, Simulia, 2009.
- [9] ANSYS, Inc., Ansys academic research mechanical, release 18.2.
URL <http://www.ansys.com/>
- [10] F. Faccio, G. Cervelli, Radiation-induced edge effects in deep submicron cmos transistors, IEEE Transactions on Nuclear Science 52 (6) (2005) 2413–2420. doi:10.1109/TNS.2005.860698.
- [11] F. Faccio, H. J. Barnaby, X. J. Chen, D. M. Fleetwood, L. Gonella, M. McLain, R. D. Schrimpf, Total ionizing dose effects in shallow trench isolation oxides, Microelectronics Reliability 48 (7) (2008) 1000 – 1007, 2007 Reliability of Compound Semiconductors (ROCS) Workshop. doi:<https://doi.org/10.1016/j.microrel.2008.04.004>.
URL <http://www.sciencedirect.com/science/article/pii/S0026271408000826>